Check for updates

Pore environment reinforced laser dye fluorescence in an adenine-containing metal–organic framework with pocket-like channels†

Li-Li Xu, [ID] [a,c] Hong Cai, [ID] *[a] Dong Luo, [ID] [b] Mian Li, [ID] [c] Yong-Liang Huang, [ID] [d] Jie-Ji Zhu,[a] Mo Xie, [ID] [b] Zi-Wei Chen[a] and Dan Li [ID] *[b]

Two novel adenine-containing metal–organic frameworks (MOFs) with the same components but different pore environments and topologies, named ZnTDCA-1 and ZnTDCA-2, were designed and synthesized. The host–guest composites were successfully fabricated by encapsulating a laser dye, 4-(*p*-dimethylaminostyryl)-1-methylpyridinium (DSM), into the MOFs, and their luminescence behaviours were found to be dependent on their different pore shapes, supported by spectral measurements, pore metrics analysis, and periodic density functional theory calculations. Notably, the quantum yield of DSM@ZnTDCA-1 can reach 39.3%, with no obvious decrease when increasing the content of DSM, indicating a favourable pore matching effect between the pocket-like pores of the ZnTDCA-1 host and DSM, which facilitates DSM to be fixed within the frameworks and uniformly dispersed. In contrast, although ZnTDCA-2 has a larger size to adsorb more dye, DSM diffuses along one-dimensional square channels after entering the host framework, resulting in the accumulation of DSM in large and regular channels, leading to fluorescence quenching. The work reveals the influence of pore shape, in particular the pocket-like confinement space, on the luminescence of the DSM@MOF system. Moreover, our preliminary cell culture and cytotoxicity experiments indicate that the DSM@MOF system is biocompatible and can serve as a platform for biological microlasers and various bio-applications.

Introduction

Metal–organic frameworks (MOFs) are a highly versatile family of organic–inorganic hybrid porous materials[1–3] that have garnered significant attention in diverse fields such as luminescence sensing,[4–6] information anticounterfeiting,[7,8] hydrocarbon separation,[9,10] and energy storage.[11,12] In recent years,

[a]School of Chemical and Environmental Engineering, Hanshan Normal University, Chaozhou, Guangdong 521041, P. R. China. E-mail: tiddychen@163.com
[b]College of Chemistry and Materials Science, Guangdong Provincial Key Laboratory of Functional Supramolecular Coordination Materials and Applications, Jinan University, Guangzhou 510632, P. R. China. E-mail: danli@jnu.edu.cn
[c]College of Chemistry and Chemical Engineering, Shantou University, and Chemistry and Chemical Engineering Guangdong Laboratory, Guangdong, 515063, P. R. China
[d]Department of Medicinal Chemistry, Shantou University Medical College, Shantou, Guangdong 515041, P. R. China
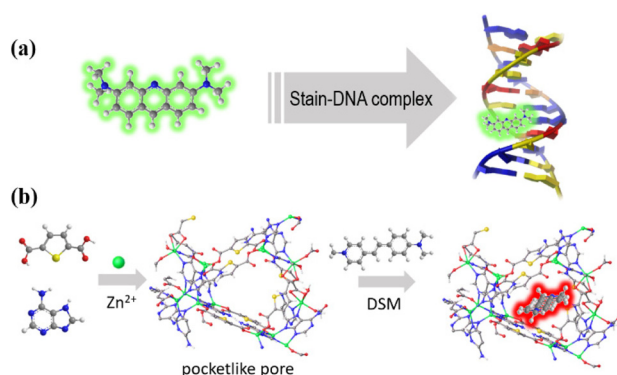
†Electronic supplementary information (ESI) available: Materials and instruments, crystal data and structural analysis, and physical measurements (FTIR, ^{1}H NMR, PXRD, TGA, N₂ adsorption, UV-Vis absorption spectra, photoluminescence, lifetime fitting, quantum yield, *etc.*). CCDC 2225750 for ZnTDCA-1 and 2225751 for ZnTDCA-2. For ESI and crystallographic data in CIF or other electronic format see DOI: https://doi.org/10.1039/d3qi01569f

the introduction of biomolecular ligands into MOFs has led to the discovery and development of biological metal–organic frameworks (BioMOFs).[13–17] These BioMOFs not only inherit the advantages of traditional MOFs but also exhibit unique superiority, enabling them to find applications in biomimetic catalysis,[18,19] DNA mimicking,[20,21] intracellular imaging,[22] clinical diagnosis and treatment.[23,24] One fascinating aspect of these MOFs is their ability to stabilize and/or confine functional species, such as nanoparticles and fluorescent dye molecules, within their porous structures and give rise to exceptional luminescence properties through host–guest interactions.[25–27] For example, confinement of a pyridinium hemicyanine dye into bio-MOF-1 results in a synergistic two-photon-pumped lasing functionality;[25] immobilization of acriflavine into the nano-channels of a BioMOF can enable it to act as a host–guest chemopalette and fluorescence ratio thermometer.[26,27] However, not all guests are stable and dispersed in the MOF matrix. It is expected that the confinement effect of MOFs with a cavity diameter slightly larger than the guest molecule is significant for achieving such a purpose.

4-(*p*-Dimethylaminostyryl)-1-methylpyridinium (DSM) is a cationic pyridinium hemicyanine dye with a linear D–π–A con-

6860 | *Inorg. Chem. Front.*, 2023, **10**, 6860–6868

This journal is © the Partner Organisations 2023

jugate structure and large first-order hyperpolarizability.[28] These kinds of organic dyes are highly sensitive to the micro-environment and can serve as potential microlasers to detect tiny changes for application in protein conformation detection and monitoring biological processes. Especially, microlasers with good biocompatibility have attracted more and more attention in the fields of photonics, medicine, sensing, biological imaging and so on due to their high resolution and high sensitivity.[29–32] However, DSM usually exhibits weak luminescence in the solid state due to the aggregation-induced quenching effect,[33] and its fluorescence efficiency can be significantly improved by incorporating it into a DNA duplex or dispersing into a porous polymer.[34–36] Our previous studies have shown dipole–dipole interaction between Watson–Crick sites of BioMOFs and dye molecules, similar to the interaction of a stain with DNA. Thus, MOFs with prominent open sites are suitable for encapsulating guest molecules.[20,26,27] Taking into account the above factors, in this work, we present the design and synthesis of a novel adenine-containing MOF with pocket-like pores[37] and Watson–Crick sites, namely ZnTDCA-1 (H_2TDC = 2,5-thiophenedicarboxylic acid, A = adenine). By analogy to the stain–DNA complex, we envisage that the DSM@BioMOF system would be capable of solving the quenching problem of DSM through pore confinement (Scheme 1). It should be noted that the pore size and shape are crucial in this context. To demonstrate the unique pore matching effect of ZnTDCA-1, another MOF with identical components, referred to as ZnTDCA-2, was successfully obtained by manipulating the reaction conditions. We explore their adsorptive luminescence behaviours and show that the distinct fluorescence properties exhibited by DSM@ZnTDCA-1 and DSM@ZnTDCA-2 are attributed to their unique aperture and channel environments. This research underscores the potential of MOFs as effective platforms for guest encapsulation and sheds light on the significant influence of pore metrics on solving the quenching problem of laser dyes.

Scheme 1 Conceptual analogy between a stain–DNA complex and the DSM@BioMOF system. (a) Illustration of the interaction between acridine orange stain and DNA showing green fluorescence. (b) Schematic representation of DSM showing red fluorescence within the confined space of the pocket-like pore in ZnTDCA-1.

Results and discussion

Single-crystal X-ray diffraction analysis reveals that ZnTDCA-1 crystallizes in the monoclinic space group $C2/c$ (Table S2†). Its asymmetric unit consists of 4 crystallographically independent Zn(II), two half TDC, three adenine (Ade), half $HCOO^-$ and one H_2O. Zn1 had a tetrahedral geometry formed by two carboxylate O atoms from two TDC^{2-} and two N7 atoms from two Ade. Zn3 and Zn4 were bridged by three Ade ligands at N3 and N9 to form a paddle-wheel $Zn_2(Ade)_3$ secondary building unit (SBU), both of which further complete the tetrahedral coordination geometry by individually bonding to an O atom from TDC^{2-}. Zn2 is six-coordinated with N1 and N7 atoms from two individual Ade, two carboxylate O atoms from a TDC^{2-}, one $HCOO^-$, and one coordinated H_2O. One-third of Ade ligands adopt a μ_4-N1:N3:N7:N9 coordination mode, while two-thirds of them adopt a μ_3-N3:N7:N9 coordination mode, leaving the Watson–Crick faces exposed (Fig. 1a). ZnTDCA-1 exhibits a 1D channel with a diameter of ca. 5.0×9.0 Å^2 and 4.5×8.5 Å^2 along the c axis. The detailed inside view is integrated with the coloured Connolly surface[38–40] (Watson–Crick faces in blue) to highlight the pocket-like pore. Interestingly, the Watson–Crick faces between two Ade on the wall of the channel form a typical double hydrogen bond, and the other H atom of the exocyclic –NH$_2$ forms a hydrogen bond with the uncoordinated carboxylate O, thus increasing the stability of the framework (Fig. 1c and S5a, b†). PLATON calculations revealed that the guest accessible volume of ZnTDCA-1 is about 35.0%, filled with $(C_2H_5)_2NH_2^+$ ions, H_2O, and DEF molecules, as inferred from elemental analysis (EA) and thermogravimetric analysis (TGA). Topological analysis of the network reveals a (4,4,6)-c net with the point symbol of $\{4\cdot5\cdot6^3\cdot8\}\{4^2\cdot5^2\cdot6^2\}\{4^3\cdot5^2\cdot6^8\cdot7\cdot8\}$ and transitivity 3 8 (meaning with 3 kinds of nodes and 8 kinds of links, Fig. 1e and S3†), which is a new 3-periodic net checked using Systre and ToposPro.[41–43]

Compared with ZnTDCA-1, ZnTDCA-2 has higher symmetry and larger pore diameter. ZnTDCA-2 crystallizes in the tetragonal space group $I4/mmm$ (Table S2†) and contains one crystallographically independent Zn(II), 0.75 TDC^{2-}, 0.5 Ade and 0.25 OH^-. As shown in Fig. 1b, the Ade ligand is disordered seriously and folded on itself. It coordinates with the central Zn(II) atom through a μ_4-N1:N3:N7:N9 coordination mode. All Zn centres have a tetrahedral coordination geometry. Two Zn1 were bridged by a hydroxyl O atom and two Ade at N3 and N9 to form a $Zn_2O(Ade)_2$ SBU, both of which are extended via linking the monodentate carboxyl groups of TDC^{2-}. Zn2 is co-ordinated by monodentate carboxyl O atoms of two TDC^{2-}, and N1 and N7 atoms from two individual Ade. Unlike ZnTDCA-1, all the Watson–Crick sites in the $Zn_2O(Ade)_2$ SBU of ZnTDCA-2 are occupied by metal atoms. This SBU further extended by coordinating with Zn2, forming large 1D channels with two square cavities of different sizes, 21×21 Å^2 and 10×10 Å^2, along the c axis. An internal view of the Connolly surface in the channel emphasizes its square aperture (Fig. 1d and S5c†). The vacancies are filled with $(CH_3)_2NH_2^+$, DMF and H_2O, as inferred from EA and TGA. The total solvent accessible

This journal is © the Partner Organisations 2023

Inorg. Chem. Front., 2023, **10**, 6860–6868 | **6861**

Fig. 1 Coordination environments (a), perspective view of the 3D framework along the *c* axis and an inside view integrated with the Connolly surface (probe radius: 1.0 Å, the same as below) shown in the orange oval box (c), and topological representation (e) of ZnTDCA-1. Coordination environments (b), perspective view of the 3D framework along the *c* axis and an inside view integrated with the Connolly surface shown in the orange circular box (d), and topological representation (f) of ZnTDCA-2. Colour codes: Zn, green; C, gray; N, blue; O, red; S, yellow; H atoms are omitted for clarity.

volume calculated using PLATON is about 60.4% of the unit cell volume. From the topological point of view, the total framework can be simplified as a (3,4,4)-c net with the point symbol of $\{4\cdot6^4\cdot7\}_2\{6\cdot7^2\}_2\{7^4\cdot8\cdot11\}$ and transitivity 3 4 (Fig. 1f and S4†), which is also a new net. Note that this is a minimal transitivity net (the simplest possible for this case), while the net for ZnTDCA-1 (transitivity 3 8) falls out of the minimal transitivity principle.[41,44,45] Being aware of quite a few situations like this, we call attention to the design and synthesis of MOFs with non-minimal transitivity nets.

ZnTDCA-1 exhibits excellent thermal stability and solvent resistance. The TGA curve and the unchanged pattern of variable temperature powder X-ray diffraction (PXRD) confirmed that the framework remained intact after the as-synthesized

sample was heated above 330 °C in air or immersed in organic solvents or H_2O (pH = 3–11) for a week (Fig. S10, S12a and S14a†). ZnTDCA-2 shows weaker stability than ZnTDCA-1. Variable temperature PXRD of ZnFDCA-2 started to change when heated to 50 °C (Fig. S12b†), and TGA showed that ZnFDCA-2 frameworks began to collapse around 275 °C (Fig. S14b†). However, ZnTDCA-2 is stable in common organic solvents except for H_2O (Fig. S11†). One of the most noteworthy features of BioMOFs is their biocompatibility. Therefore, *in vitro* toxicity experiments of ZnTDCA-1 and ZnTDCA-2 were conducted using normal human fetal lung fibroblast 1 (HFL1) and human esophageal cancer cells (KYSE150) using CCK8 assays.[46] The results showed that after 48 h of exposure to ZnTDCA-1 and ZnTDCA-2, the cell viability of HFL1 and KYSE150 remained above 96%, even when the BioMOF concentration was increased to 150 μg mL^{-1} (Fig. S23†), demonstrating the good biological compatibility of ZnTDCA-1 and ZnTDCA-2, which meets a prerequisite for potential biological applications.

Both ZnTDCA-1 and ZnTDCA-2 emitted weak blue-violet photoluminescence in the solid state under UV light irradiation (excited at 365 nm). Fig. 2 shows the emission and excitation spectra of ZnTDCA-1 and ZnTDCA-2. At ambient temperature, their maximum emission wavelengths are located at about 423 nm (λ_{ex} = 380 nm) and 435 nm (λ_{ex} = 375 nm), respectively. Interestingly, at 78 K, both ZnTDCA-1 and ZnTDCA-2 show obvious dual-emission behaviour (λ_{ex} = 320 nm) with a strong emission peak located near 530–540 nm and a weak peak emission peak located at about 414 nm. To confirm the origin of the emission, we obtained the emission
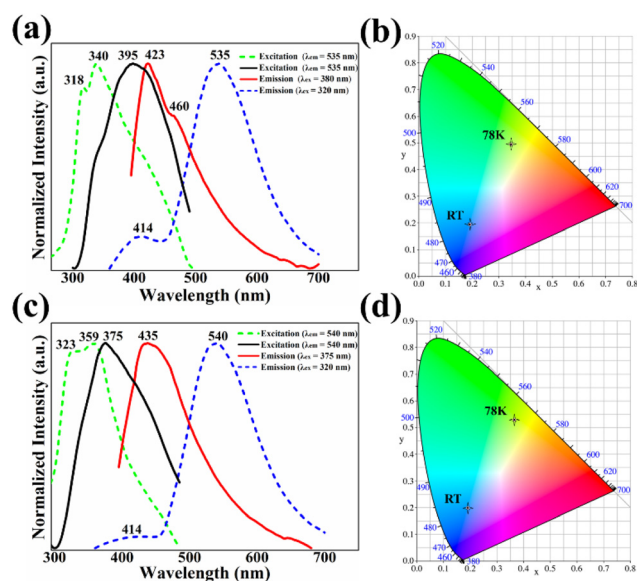

Fig. 2 The solid excitation and emission spectra of ZnTDCA-1 (a) and ZnTDCA-2 (c) at ambient temperature (solid lines) and 78 K (dashed lines). The corresponding CIE chromaticity diagrams showing the luminescence colours of ZnTDCA-1 (b) and ZnTDCA-2 (d) at ambient temperature and 78 K.

6862 | *Inorg. Chem. Front.*, 2023, **10**, 6860–6868

This journal is © the Partner Organisations 2023

spectra of free Ade and H$_2$TDC under similar conditions (Fig. S17 and S18†). At ambient temperature, the maximum emission wavelengths of free adenine and H$_2$TDC are approximately 410 nm (with a shoulder at about 462 nm) and 450 nm (broad peak), respectively. At 78 K, the emission peaks of Ade and H$_2$TDC are at about 430 nm and 543 nm, respectively, which correspond to the dual-emission of ZnTDCA-1 and ZnTDCA-2. Meanwhile, the UV-Vis absorption spectra of ZnTDCA-1, ZnTDCA-2, Ade and H$_2$TDC were recorded (Fig. S16†). The absorption spectra featured intense broad bands centred at 250–300 nm and 250–310 nm for ZnTDCA-1 and ZnTDCA-2, respectively, which coincide with the ultra-violet absorption peaks reported for free Ade (250–290 nm) and H$_2$TDC (250–315 nm). Therefore, we reasonably believe that the emission of ZnTDCA-1 and ZnTDCA-2 can be assigned to the metal-mediated intraligand π–π* transition of Ade and/or H$_2$TDC ligands that surround the Zn(II). This means that ZnTDCA-1 and ZnTDCA-2 retained the temperature-sensitive nature of the thiophene ligand and some properties of the adenine ligand.[26]

DSM dye was successfully synthesized according to the method reported in the literature[25] with a slight modification (Scheme S1 and Fig. S9†), and then it was incorporated into the two BioMOFs to form DSM@BioMOF. Upon immersing the as-prepared crystals of ZnTDCA-1 (or ZnTDCA-2) into a DMF solution with varying concentrations of DSM, the color of the crystal changed quickly from the original colourless ZnTDCA-1 (or ZnTDCA-2) to red DSM@ZnTDCA-1 (or DSM@ZnTDCA-2), while the color of the solvent faded. Such a phenomenon was easily discerned visually and authenticated using UV-Vis absorption spectroscopy. Moreover, as the adsorbed dye content increased, the color of the dye@MOF composite evolved from a bright red to a darker shade (Fig. S1†). The PXRD pattern of DSM@ZnTDCA-1 (or DSM@ZnTDCA-2) obtained by ion exchange is basically consistent with the diffraction pattern of ZnTDCA-1 (or ZnTDCA-2), indicating that the crystalline integrity of host frameworks remained unchanged (Fig. S13†). To ascertain the infiltration of the dye in the channels of BioMOFs, we conducted an N$_2$ adsorption experiment, selecting ZnTDCA-1 as the sample of focus. As shown in Fig. S15a,† the N$_2$ adsorption capacity of ZnTDCA-1 is about 126 cm^3 g^{-1} at 77 K, while that of DSM@ZnTDCA-1 is only 59 cm^3 g^{-1}. On the other hand, the pore size of ZnTDCA-1 decreased from 6.79 to 5.90 Å (Fig. S15c†). By combining the infrared spectrum containing structural information of DSM dye (1581 cm^{-1} for $\delta_{C=N}$, $\delta_{C=C}$ and 1163 cm^{-1} for δ_{C-N}, δ_{C-C}, Fig. S7†), fluorescence spectroscopy (PL), UV-Vis spectrophotometry (UV-Vis), and the color of a series of DSM@MOF composites (Tables S1, S4 and Fig. S1, S2†), we conclude that DSM has been successfully encapsulated into both frameworks. Utilizing both PL and UV-Vis methods, the content of dye within the composites was determined, and the values were almost the same. The maximum adsorption capacity was approximately 780 mg g^{-1} for ZnTDCA-1 and 3150 mg g^{-1} for ZnTDCA-2. Dye desorption experiments were performed according to the methods

reported in the literature.[20] The result showed that the DSM in ZnTDCA-2 desorbed faster than that in ZnTDCA-1, with 85% of the DSM released within 18 h, whereas only 36% of the DSM in ZnTDCA-1 released simultaneously, suggesting the inter-action between the open Watson–Crick sites in the ZnTDCA-1 framework and DSM (Fig. S22a†). To assess the stability of the DSM@BioMOF system in biologically relevant media, we immersed it in phosphate buffered saline (PBS) solutions and found that the washed DSM@ZnTDCA-1 showed little dye leaching, whereas DSM@ZnTDCA-2 showed a distinct color change. This indicates that DSM@ZnTDCA-1 has good biosol-vent stability and has not undergone chemical transformation, as evidenced by UV-Vis spectra and PXRD (Fig. S22b and S13†). TGA showed that DSM adsorption did not reduce their thermal stability (Fig. S14†).

To explore the influence of the host frameworks on the guest molecule, we performed fluorescence emission spectroscopy of DSM in liquid (1.0 × 10^{-6} M) and solid states. As shown in Fig. 3 and Fig. S19,† both of them exhibit weak emission, with maximum emission peaks at 623 nm and 667 nm, respectively. When the concentration of DSM is low (around 0.01 wt%), DSM@ZnTDCA-1 and DSM@ZnTDCA-2 exhibit strong luminescence, displaying the characteristic emissions
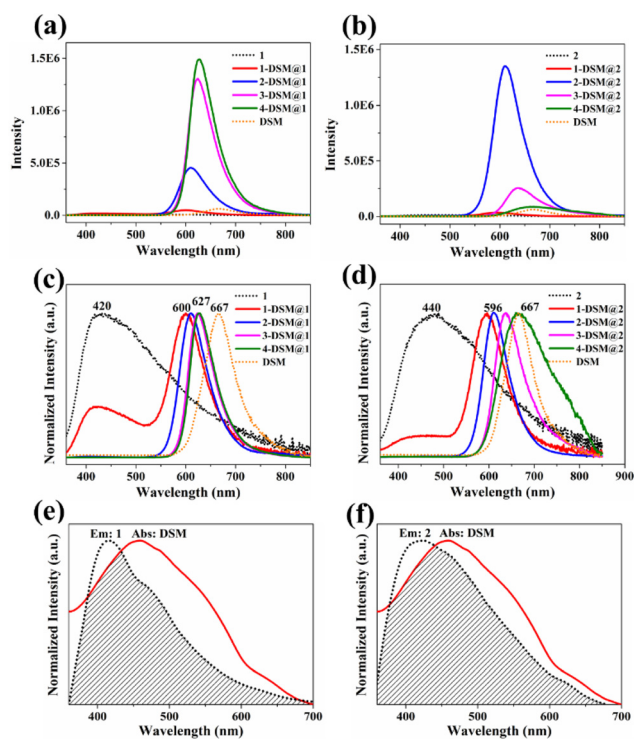

Fig. 3 (a) The solid emission spectra of DSM, 1 (i.e. ZnTDCA-1) and a series of DSM@ZnTDCA-1 with different dye loading amounts; (b) the solid emission spectra of DSM, 2 (i.e. ZnTDCA-2) and a series of DSM@ZnTDCA-2 with different dye loading amounts; (c) and (d) show the normalized results of emission intensity for (a) and (b), respectively; (e) and (f) the black shaded areas are the overlap of the absorbance spectrum of DSM and emission spectra of 1 and 2, respectively. The unified excitation wavelength is 340 nm.

This journal is © the Partner Organisations 2023

Inorg. Chem. Front., 2023, 10, 6860–6868 | 6863

of both the guest (λ_{em} = 600 nm) and host moieties (λ_{em} = 420 nm for ZnTDCA-1, λ_{em} = 440 nm for ZnTDCA-2) upon excitation at 340 nm. The luminous colors of the DSM@ZnTDCA-1 and DSM@ZnTDCA-2 composites can be adjusted by varying the content of the guest DSM in the host frameworks from orange to red (Fig. S20†). Furthermore, the emission intensity of DSM is significantly enhanced with increasing amounts of encapsulated DSM in the DSM@ZnTDCA-1 composite system (for DSM@ZnTDCA-2, the emission intensity increased at first and then decreased because of aggregation quenching with increasing content of DSM). Notably, the maximum emission wavelength was redshifted (from 600 to 627 nm for DSM@ZnTDCA-1, and 596 to 667 nm for DSM@ZnTDCA-2), which is similar to the luminescence behavior between adenine-based ZnBDCA and acriflavine,[26] suggesting the possibility of host–guest electron/energy transfer (Fig. 3c and d). As expected, there is spectral overlap between the absorption of DSM and the emission of ZnTDCA-1 (or ZnTDCA-2), which is necessary for resonance energy transfer (Fig. 3e and f). To confirm the potential energy transfer between the host and the guest, we measured the fluorescence lifetime of ZnTDCA-1, ZnTDCA-2, DSM@ZnTDCA-1 and DSM@ZnTDCA-2 and subsequently estimated the energy transfer efficiency (Φ_{ET}) for each compound (Tables S3 and S4†). As the DSM dye content increased from 0.01 to 0.78 wt% (or from 0.01 to 3.15 wt%), there was a corresponding increase in energy transfer from the donor ZnTDCA-1 (or ZnTDCA-2) to the acceptor DSM. The Φ_{ET} of DSM@ZnTDCA-1 (or DSM@ZnTDCA-2) gradually increased from 43.50% to 92.86% (or from 16.55% to 93.01%), indicating a higher efficiency of energy transfer upon guest loading.

The unique adsorptive luminescence behavior of DSM cationic ions within the confined spaces of ZnTDCA-1 and ZnTDCA-2 pores was further investigated using *in situ* fluorescence microscopy. For ZnTDCA-1, bright-red emission occurred gradually from external faces to the inside of the crystal. Finally, the entire crystal displayed strong red emission after 1 h, and no obvious luminescence quenching was observed after soaking in the DSM solution for 32 h (Fig. 4e and S21a†). For ZnTDCA-2, it can be deduced from the dynamic changes of the luminescence region that DSM diffuses along the 1D channel direction in ZnTDCA-2. The terminal region of the rod-like crystal first generates red emission, and then the red luminescence region quickly extends along the longitudinal direction to the whole crystal within 1 h. With the further diffusion of dye molecules in the MOF matrix, the red emission of DSM@ZnTDCA-2 is gradually quenched from both ends to the center (Fig. 4f and S21b†). Remarkably, the quantum yield (QY) of DSM@ZnTDCA-1 showed an increasing trend with the DSM content increasing, while for DSM@ZnTDCA-2, the QY exhibited a maximum value at a certain DSM concentration before decreasing, which is consistent with the observed luminescence intensity (Fig. 3a, b and Table S4†). For ZnTDCA-1, the maximum QY of 39.3% is achieved at a high DSM content of 0.78 wt%, and no obvious fluorescence quenching is observed with the increase of DSM. For ZnTDCA-2, the maximum QY of DSM@ZnTDCA-2
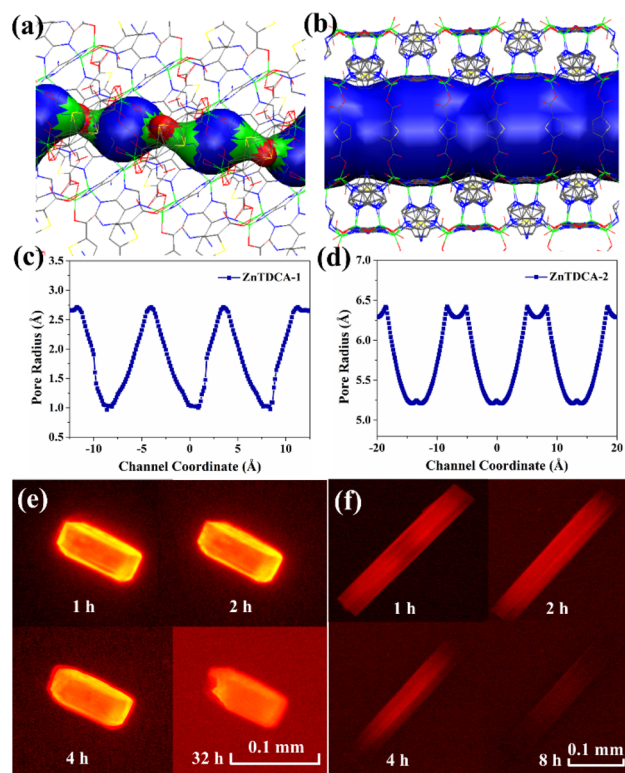

Fig. 4 (a and c) The side view of ZnTDCA-1 highlighting the shape of pocket-like pores (the blue tube indicates that the radius is double the minimum for a single guest molecule; red indicates where the pore radius is relatively tight for a water molecule; green indicates where there is room for a single water), along with pore-metrics analysis (curve in navy blue). (b and d) The side view of ZnTDCA-2 highlighting the shape of square channels, along with pore-metrics analysis (curve in navy blue). The corresponding fluorescence microscopy image evolution of DSM encapsulated into ZnTDCA-1 (e) and ZnTDCA-2 (f) (in 1.00 mg mL^{-1} DSM/DMF solution).

reached 39.9% at a DSM concentration of 0.10 wt%, while it decreased to 4.7% at a DSM concentration of 3.15 wt%.

Both ZnTDCA-1 and ZnTDCA-2 are anionic BioMOFs with similar contributions from charge effects to ion exchange. To determine the contribution of pore size and shape to the different adsorptive luminescence behavior and to visualize the spatial effect, pore-metrics analyses of ZnTDCA-1 and ZnTDCA-2 were performed using the HOLE method.[20,47,48] As shown in Fig. 4a and c, the maximum and minimum diameters of ZnTDCA-1 channels are approximately 5.6 Å and 2.0 Å, respectively, showing a helical pocket-like channel. The dimension of this channel matches the DSM molecular size (about 3.5 × 6.3 × 14.3 Å^3, according to the energy optimized molecular model),[36] indicating that the dye molecules could not move freely during adsorption or desorption due to the steric effect. The open Watson–Crick sites and uncoordinated carboxyl O present in the framework effectively restrict the rotary motion of DSM guests, and the single-molecule dispersion of DSM in the host framework restrains π–π interactions and mitigates the aggregation-caused quenching effect of DSM.[25,49] This is consistent with our observation of the adsorption luminescence behaviour and the variation trend of the quantum yield

6864 | *Inorg. Chem. Front.*, 2023, **10**, 6860–6868

This journal is © the Partner Organisations 2023

(Table S4†). In contrast, ZnTDCA-2 has a straight channel with a diameter of about 10.5 to 13 Å, in which DSM can freely shuttle without hindrance (Fig. 4b and d). The luminescence intensity of DSM@ZnTDCA-2 exhibited an initial increase and then a decrease with increasing DSM content. This phenomenon is attributed to the diffusion of DSM along one-dimensional channels upon entering the host framework, leading to fluorescence quenching due to the continuous accumulation in large and regular channels as the adsorption content increases.

To further understand the interaction between the MOF host and the dye guest, as well as the corresponding electronic structural changes after DSM embedding, periodic density functional theory (DFT) calculations were performed. The optimized structures indicate that the dye molecules of ZnTDCA-1 and ZnTDCA-2 are incorporated into a larger pocket-like cavity and a square channel (Fig. S24†). In DSM@ZnTDCA-1, DSM exhibits a close interaction configuration with the ZnTDCA-1 framework due to size matching, whereas DSM can only interact with the exposed thiophene groups in ZnTDCA-2. Analysis of the differences in charge densities based on the optimized interaction configurations revealed significant charge transfer from DSM to the overall ZnTDCA-1 framework. On the other hand, in DSM@ZnTDCA-2, the charge transfer is localized on the DSM molecule and the adjacent thiophene group. Therefore, the main reason for the fluorescence enhancement in ZnTDCA-1 may be attributed to the effective charge transfer and structural restriction originating from DSM to ZnTDCA-1.

Conclusions

In summary, two new nucleobase-containing MOFs, ZnTDCA-1 and ZnTDCA-2, with different pore environments and topological nets were elaborately obtained by varying the synthesis conditions. The dual-emission DSM@BioMOF composites have been prepared successfully by encapsulating the fluorescent dye DSM into BioMOFs, and their different adsorption luminescence behaviors have been investigated. Interestingly, despite the larger aperture of ZnTDCA-2, the size matching and abundant open sites of ZnTDCA-1 allow DSM to be uniformly dispersed into the pocket-like pores, resulting in the DSM@ZnTDCA-1 system having a high quantum yield (~39%) at 340 nm. This work demonstrates the significant role of confined space, charge transfer, and energy transfer in enhancing the luminescence properties of dyes in MOFs, which, combined with the biocompatibility of BioMOFs, can be used as potential microlasers to detect subtle changes in biological systems. It also provides new ideas for the design and development of potential platforms for efficient light-emitting materials in various applications.

Experimental section

Synthesis of ZnTDCA-1

A mixture of $Zn(NO_3)_2 \cdot 6H_2O$ (0.09 mmol), 2,5-thiophenedicarboxylic acid (H_2TDC, 0.05 mmol), and adenine (Ade, 0.06 mmol) was dissolved in a mixed solvent of N,N-diethylformamide (DEF) and ethanol (4.0 mL, 2 : 2, v/v) with the addition of drops of HNO_3 (0.64 mol L^{-1}, 0.80 mL). The solution was then sealed in a Pyrex glass tube and heated in an oven at 100 °C for 72 h and cooled to room temperature at a rate of 5 °C h^{-1}. Colourless prism crystals were filtered off and dried. Yield: *ca.* 69% based on Ade. FTIR spectrum (KBr pellets, cm^{-1}): 3347 (m, b), 3153 (m, b), 2926 (w), 2855 (w), 1664 (vs), 1613 (vs), 1576 (s), 1531 (m), 1478 (m), 1415 (s), 1358 (vs), 1301 (vs), 1226 (s), 1161 (s), 1109 (w), 1028 (w), 811 (w), 795 (m), 767 (m), 746 (m), 649 (w), 586 (w), 568 (w), 509 (w) (Fig. S6 and S7a†). Elemental analysis (CHNS), $(C_{80}H_{92}N_{34}O_{31}S_5Zn_8)_n$, that is, $\{(C_2H_5)_2NH_2 \cdot [(Zn_8(H_2O)_2(HCOO)(Ade)_6(TDC)_5)] \cdot 4H_2O \cdot 3DEF\}_n$, calculated (%): C, 35.47; H, 3.42; N, 17.58; S, 5.92; found (%): C, 35.51; H, 3.25; N, 17.71; S, 6.14. ^1H NMR of digested ZnTDCA-1, calculated: Ade/TDC ratio, 1 : 0.83 (based on SXRD); found, 1 : 0.82 (Fig. S8†).

Synthesis of ZnTDCA-2

A mixture of $Zn(NO_3)_2 \cdot 6H_2O$ (0.09 mmol), H_2TDC (0.06 mmol), and Ade (0.04 mmol) was dissolved in a mixed solvent of N,N-dimethylformamide (DMF) and ethanol (6 mL, 2.5 : 3.5, v/v) with the addition of drops of HNO_3 (0.64 mol L^{-1}, 0.55 mL). The solution was then sealed in a Pyrex glass tube and heated in an oven at 120 °C for 72 h and cooled to room temperature at a rate of 5 °C h^{-1}. Colourless rod crystals were filtered off and dried. Yield: *ca.* 65% based on Ade. FTIR spectrum (KBr pellets, cm^{-1}): 3344 (m, b), 3178 (m, b), 2921 (w), 2851 (w), 2796 (m), 1661 (vs), 1604 (vs), 1528 (s), 1470 (m), 1352 (vs), 1215 (m), 1156 (m), 1107 (w), 1023 (w), 808 (w), 769 (m), 568 (w) (Fig. S6 and S7b†). Elemental analysis (CHNS), $(C_{36}H_{54}N_{13}O_{23.5}S_3Zn_4)_n$, that is $\{(CH_3)_2NH_2 \cdot [Zn_4(Ade)_2(TDC)_3(OH)] \cdot 8.5H_2O \cdot 2DMF\}_n$, calculated (%): C, 30.83; H, 3.88; N, 12.98; S, 6.86; found (%): C, 30.92; H, 3.73; N, 13.25; S, 7.00. ^1H NMR of digested ZnTDCA-2, calculated Ade/TDC ratio, 1 : 1.50 (based on SXRD); found, 1 : 1.49 (Fig. S8†).

Synthesis of DSM@MOF composites

Crystals of ZnTDCA-1 (or ZnTDCA-2) were immersed in DSM/DMF solution with varying concentrations from 1.0×10^{-6} to 1.0×10^{-3} mol L^{-1} at ambient temperature for 3 days to yield a series of DSM@ZnTDCA-1 (or DSM@ZnTDCA-2) composites with different DSM contents. They are, in turn, abbreviated as 1-DSM@1, 2-DSM@1, 3-DSM@1 and 4-DSM@1 (or 1-DSM@2, 2-DSM@2, 3-DSM@2 and 4-DSM@2). The products were washed thoroughly with DMF to remove residual DSM on the surface of BioMOFs and dried at 60 °C for 1 h (Fig. S1†).

DSM release experiments

10 mg of ZnTDCA-1 (or ZnTDCA-2) sample was immersed in 2 mL of 1.5×10^{-5} mol L^{-1} DSM/DMF solution for 1.5 h; the solution changed from red to colorless and showed zero absorbance when tested with liquid UV-Vis absorption spectroscopy. After the completion of the uptake process, the release experiments were carried out. 2 mL of $Zn(NO_3)_2$/DMF solution (0.1 mol L^{-1}) was used to replace the above colorless solution; the soaked sample

This journal is © the Partner Organisations 2023

Inorg. Chem. Front., 2023, **10**, 6860–6868 | **6865**

was kept at 50 °C to speed up the desorption process, and the absorbance was measured every 6 h to monitor the desorption of DSM. 2 mg of 0.78 wt% DSM@ZnTDCA-1 or 3.15 wt% DSM@ZnTDCA-2 were immersed in 2 mL of PBS solution for 2, 12, and 24 h. The absorption spectra were obtained to observe the biological stability of DSM@ZnTDCA-1 and DSM@ZnTDCA-2; 15 μmol L^{-1} DSM/PBS solution was used as the reference.

Cell culture and cytotoxicity experiments

The cytotoxicity of ZnTDCA-1 and ZnTDCA-2 was evaluated using a CCK8 assay kit (Absin, China). In a 96-well plate, human fetal lung fibroblast 1 (HFL1) cells were incubated in Ham's F-12K + 10% fetal bovine serum (FBS) + 1% penicillin/streptomycin (P/S), and KYSE150 human esophageal cancer (KYSE 150) cells were incubated in 48.5% RPMI-1640 + 48.5% F-12 + 2% FBS + 1% P/S, in a humidified incubator (37 °C, 5% CO_2). After 48 h for the above HFL1 (or 24 h for KYSE 150), ZnTDCA-1 (or ZnTDCA-2) at different concentrations (0, 30, 60, 90, 120 and 150 μg mL^{-1}) were added to each well and incubated for another 48 h, respectively. Next, 10% CCK8 solution was added to each test well and incubated for 1 h. The absorbance of each sample at 450 nm was measured using a microplate reader. The cell viability was calculated as the ratio of sample absorbance/control and expressed as a percentage. All experiments were performed in parallel three times and averaged.

Computational details

All calculations were performed with the Vienna *Ab initio* Simulation Package (VASP)[50] employing the generalized gradient approximation (GGA)[51] using the PBE formulation.[52] The projected augmented wave (PAW) potentials[53] were chosen to describe the ionic cores and valence electrons were taken into account using a plane wave basis set with a kinetic energy cutoff of 400 eV. Partial occupancies of the Kohn Sham orbitals were allowed using the Gaussian smearing method and a width of 0.05 eV. The electronic energy was considered self-consistent when the energy change was smaller than 2×10^{-5} eV. The geometry optimization was considered convergent when the force change was smaller than 0.02 eV A^{-1}. The analysis of charge density difference was accomplished by the subtraction of the charge density between DSM@MOF and isolated DSM and MOF.

Author contributions

L.-L. Xu and H. Cai conceived and wrote the manuscript and supervised the research; D. Li supervised the research and polished the manuscript; L.-L. Xu, D. Luo, J.-J. Zhu, and Z.-W. Chen conducted the synthesis, PXRD, UV-Vis, TG, IR, EA, fluorescence, cell culture and cytotoxicity experiments and analyses; M. Li participated in the discussion of the manuscript and contributed to the topological analysis; Y.-L. Huang contributed to SCXRD analysis; and M. Xie conducted the theore-

tical calculation. All authors read and commented on the manuscript.

Conflicts of interest

There are no conflicts to declare.

Acknowledgements

References

1 H. Furukawa, K. E. Cordova, M. O'Keeffe and O. M. Yaghi, The Chemistry and Applications of Metal–Organic Frameworks, *Science*, 2013, **341**, 1230444.

2 M. Ahmed, Recent advancement in bimetallic metal organic frameworks (M'MOFs): synthetic challenges and applications, *Inorg. Chem. Front.*, 2022, **9**, 3003–3033.

3 Y. Liu, J. Dai, L. Guo, Z. Zhang, Y. Yang, Q. Yang, Q. Ren and Z. Bao, Porous Hydrogen-Bonded Frameworks Assembled from Metal-Nucleobase Entities for Xe/Kr Separation, *CCS Chem.*, 2022, **4**, 381–388.

4 B. Gui, X. Liu, G. Yu, W. Zeng, A. Mal, S. Gong, C. Yang and C. Wang, Tuning of Förster Resonance Energy Transfer in Metal–Organic Frameworks: Toward Amplified Fluorescence Sensing, *CCS Chem.*, 2020, **2**, 2054–2062.

5 S. Wang, B. Sun, Z. Su, G. Hong, X. Li, Y. Liu, Q. Pan and J. Sun, Lanthanide-MOFs as multifunctional luminescent sensors, *Inorg. Chem. Front.*, 2022, **9**, 3259–3266.

6 L.-L. Xu, Q.-F. Zhang, D. Wang, G.-W. Wu and H. Cai, Construction of a Luminescent Cadmium-Based Metal–Organic Framework for Highly Selective Discrimination of Ferric Ions, *Molecules*, 2021, **26**, 6847.

7 J. I. Deneff, K. S. Butler, L. E. S. Rohwer, C. J. Pearce, N. R. Valdez, M. A. Rodriguez, T. S. Luk and D. F. Sava Gallis, Encoding Multilayer Complexity in Anti-Counterfeiting Heterometallic MOF-Based Optical Tags, *Angew. Chem., Int. Ed.*, 2021, **60**, 1203–1211.

6866 | *Inorg. Chem. Front.*, 2023, **10**, 6860–6868

This journal is © the Partner Organisations 2023

8 H. Zhou, J. Han, J. Cuan and Y. Zhou, Responsive luminescent MOF materials for advanced anticounterfeiting, *Chem. Eng. J.*, 2022, **431**, 134170.

9 G.-D. Wang, R. Krishna, Y.-Z. Li, Y.-Y. Ma, L. Hou, Y.-Y. Wang and Z. Zhu, Rational Construction of Ultrahigh Thermal Stable MOF for Efficient Separation of MTO Products and Natural Gas, *ACS Mater. Lett.*, 2023, **5**, 1091–1099.

10 H. Zeng, M. Xie, T. Wang, R.-J. Wei, X.-J. Xie, Y. Zhao, W. Lu and D. Li, Orthogonal-array dynamic molecular sieving of propylene/propane mixtures, *Nature*, 2021, **595**, 542–548.

11 Y. Peng, J. Xu, J. Xu, J. Ma, Y. Bai, S. Cao, S. Zhang and H. Pang, Metal-organic framework (MOF) composites as promising materials for energy storage applications, *Adv. Colloid Interface Sci.*, 2022, **307**, 102732.

12 X. Zhang, R.-B. Lin, Z. A. Alothman, O. Alduhaish, T. Yildirim, W. Zhou, J.-R. Li and B. Chen, Promotion of methane storage capacity with metal–organic frameworks of high porosity, *Inorg. Chem. Front.*, 2023, **10**, 454–459.

13 H. Cai, Y. L. Huang and D. Li, Biological metal–organic frameworks: Structures, host-guest chemistry and bio-applications, *Coord. Chem. Rev.*, 2019, **378**, 207–221.

14 R. K. Gupta, M. Riaz, M. Ashafaq, Z.-Y. Gao, R. S. Varma, D.-C. Li, P. Cui, C.-H. Tung and D. Sun, Adenine-incorporated metal–organic frameworks, *Coord. Chem. Rev.*, 2022, **464**, 214558.

15 L.-L. Xu, H.-F. Zhang, M. Li, S. W. Ng, J.-H. Feng, J.-G. Mao and D. Li, Chiroptical Activity from an Achiral Biological Metal–Organic Framework, *J. Am. Chem. Soc.*, 2018, **140**, 11569–11572.

16 I. Imaz, M. Rubio-Martínez, J. An, I. Solé-Font, N. L. Rosi and D. Maspoch, Metal–biomolecule frameworks (MBioFs), *Chem. Commun.*, 2011, **47**, 7287–7302.

17 G. Beobide, O. Castillo, J. Cepeda, A. Luque, S. Pérez-Yáñez, P. Román and J. Thomas-Gipson, Metal–carboxylato–nucleobase systems: From supramolecular assemblies to 3D porous materials, *Coord. Chem. Rev.*, 2013, **257**, 2716–2736.

18 R.-J. Wei, H.-G. Zhou, Z.-Y. Zhang, G.-H. Ning and D. Li, Copper(I)–Organic Frameworks for Catalysis: Networking Metal Clusters with Dynamic Covalent Chemistry, *CCS Chem.*, 2020, **2**, 2045–2053.

19 Q. Li, Y. Chen, S. Bai, X. Shao, L. Jiang and Q. Li, Immobilized lipase in bio-based metal-organic frameworks constructed by biomimetic mineralization: A sustainable biocatalyst for biodiesel synthesis, *Colloids Surf., B*, 2020, **188**, 110812.

20 H. Cai, M. Li, X.-R. Lin, W. Chen, G.-H. Chen, X.-C. Huang and D. Li, Spatial, Hysteretic, and Adaptive Host–Guest Chemistry in a Metal–Organic Framework with Open Watson–Crick Sites, *Angew. Chem., Int. Ed.*, 2015, **54**, 10454–10459.

21 H. Cai, Y.-X. Wu, Z. Lu, D. Luo, J.-X. Sun, G.-W. Wu, M. Li, Y.-B. Wei, L.-M. Zhong and D. Li, Mimicking DNA Periodic Docking Grooves for Adaptive Identification of L-/ D-tryptophan in a Biological Metal-Organic Framework, *J. Am. Chem. Soc.*, 2022, **144**, 9559–9563.

22 S. Zhang, X. Pei, H. Gao, S. Chen and J. Wang, Metal-organic framework-based nanomaterials for biomedical applications, *Chin. Chem. Lett.*, 2020, **31**, 1060–1070.

23 C. Hu, J. Chen, H. Zhang, L. Wu, P. Yang and X. Hou, Nanoscale metal organic frameworks and their applications in disease diagnosis and therapy, *Microchem. J.*, 2022, **180**, 107595.

24 H. Wang, S. Li, L. Wang, Z. Liao, H. Zhang, T. Wei and Z. Dai, Functionalized biological metal–organic framework with nanosized coronal structure and hierarchical wrapping pattern for enhanced targeting therapy, *Chem. Eng. J.*, 2023, **456**, 140963.

25 J. Yu, Y. Cui, H. Xu, Y. Yang, Z. Wang, B. Chen and G. Qian, Confinement of pyridinium hemicyanine dye within an anionic metal–organic framework for two-photon-pumped lasing, *Nat. Commun.*, 2013, **4**, 2719.

26 H. Cai, L.-L. Xu, H.-Y. Lai, J.-Y. Liu, S. W. Ng and D. Li, A highly emissive and stable zinc(II) metal–organic framework as a host–guest chemopalette for approaching white-light-emission, *Chem. Commun.*, 2017, **53**, 7917–7920.

27 H. Cai, W. Lu, C. Yang, M. Zhang, M. Li, C.-M. Che and D. Li, Tandem Förster Resonance Energy Transfer Induced Luminescent Ratiometric Thermometry in Dye-Encapsulated Biological Metal–Organic Frameworks, *Adv. Opt. Mater.*, 2019, **7**, 1801149.

28 S. R. Marder, J. W. Perry and W. P. Schaefer, Synthesis of Organic Salts with Large Second-Order Optical Nonlinearities, *Science*, 1989, **245**, 626–628.

29 Y. Wei, X. Lin, C. Wei, W. Zhang, Y. Yan and Y. S. Zhao, Starch-Based Biological Microlasers, *ACS Nano*, 2017, **11**, 597–602.

30 Y. Zhang, C. Zhang, Y. Fan, Z. Liu, F. Hu and Y. S. Zhao, Smart Protein-Based Biolasers: An Alternative Way to Protein Conformation Detection, *ACS Appl. Mater. Interfaces*, 2021, **13**, 19187–19192.

31 K. J. Vahala, Optical microcavities, *Nature*, 2003, **424**, 839–846.

32 M. Humar and S. Hyun Yun, Intracellular microlasers, *Nat. Photonics*, 2015, **9**, 572–576.

33 Y. Yu, H. Xing, Z. Zhou, J. Liu, H. H. Y. Sung, I. D. Williams, J. E. Halpert, Z. Zhao and B. Z. Tang, How do molecular interactions affect fluorescence behavior of AIEgens in solution and aggregate states?, *Sci. China: Chem.*, 2022, **65**, 135–144.

34 C. Allain, F. Schmidt, R. Lartia, G. Bordeau, C. Fiorini-Debuisschert, F. Charra, P. Tauc and M.-P. Teulade-Fichou, Vinyl-Pyridinium Triphenylamines: Novel Far-Red Emitters with High Photostability and Two-Photon Absorption Properties for Staining DNA, *ChemBioChem*, 2007, **8**, 424–433.

35 H. He, Y. Cui, H. Li, K. Shao, B. Chen and G. Qian, Controllable broadband multicolour single-mode polarized

This journal is © the Partner Organisations 2023

Inorg. Chem. Front., 2023, **10**, 6860–6868 | **6867**

laser in a dye-assembled homoepitaxial MOF microcrystal, *Light: Sci. Appl.*, 2020, **9**, 138.

36 Y. Wan, L. Yu and T. Xia, A dye-loaded nonlinear metal-organic framework as self-calibrated optical thermometer, *Dyes Pigm.*, 2022, **202**, 110234.

37 Z.-S. Wang, M. Li, Y.-L. Peng, Z. Zhang, W. Chen and X.-C. Huang, An Ultrastable Metal Azolate Framework with Binding Pockets for Optimal Carbon Dioxide Capture, *Angew. Chem., Int. Ed.*, 2019, **58**, 16071–16076.

38 M. F. Sanner, A. J. Olson and J.-C. Spehner, Reduced surface: An efficient way to compute molecular surfaces, *Biopolymers*, 1996, **38**, 305–320.

39 M. F. Sanner, Python: A Programming Language for Software Integration and Development, *J. Mol. Graphics Modell.*, 1999, **17**, 57–61.

40 C.-R. Ye, W.-J. Wang, W. Chen, Y. Xiao, H.-F. Zhang, B.-L. Dai, S.-H. Chen, X.-D. Wu, M. Li and X.-C. Huang, Harnessing Shape Complementarity for Upgraded Cyclohexane Purification through Adaptive Bottlenecked Pores in an Imidazole-Containing MOF, *Angew. Chem., Int. Ed.*, 2021, **60**, 23590–23595.

41 M. Li, D. Li, M. O'Keeffe and O. M. Yaghi, Topological Analysis of Metal–Organic Frameworks with Polytopic Linkers and/or Multiple Building Units and the Minimal Transitivity Principle, *Chem. Rev.*, 2014, **114**, 1343–1370.

42 O. Delgado-Friedrichs and M. O'Keeffe, Identification of and symmetry computation for crystal nets, *Acta Crystallogr., Sect. A: Found. Crystallogr.*, 2003, **59**, 351–360.

43 V. A. Blatov, A. P. Shevchenko and D. M. Proserpio, Applied Topological Analysis of Crystal Structures with the Program Package ToposPro, *Cryst. Growth Des.*, 2014, **14**, 3576–3586.

44 M. Li, M. O'Keeffe, D. M. Proserpio and H.-F. Zhang, A New Group of Edge-transitive 3-Periodic Nets and Their Derived Nets for Reticular Chemistry, *Cryst. Growth Des.*, 2020, **20**, 4062–4068.

45 Z. Chen, H. Jiang, M. Li, M. O'Keeffe and M. Eddaoudi, Reticular Chemistry 3.2: Typical Minimal Edge-Transitive Derived and Related Nets for the Design and Synthesis of Metal–Organic Frameworks, *Chem. Rev.*, 2020, **120**, 8039–8065.

46 Y. Li, H. Zhang, C. Chen, K. Qiao, Z. Li, J. Han, X. Han, K. Li, K. Lai, N. Liu, A. Li, N. Xiao, Y. Zhang, X. Zhao, W. Gao, Y. Zhang, H. Liu and T. Sun, Biomimetic Immunosuppressive Exosomes that Inhibit Cytokine Storms Contribute to the Alleviation of Sepsis, *Adv. Mater.*, 2022, **34**, 2108476.

47 O. S. Smart, J. M. Goodfellow and B. A. Wallace, The pore dimensions of gramicidin A, *Biophys. J.*, 1993, **65**, 2455–2460.

48 O. S. Smart, J. G. Neduvelil, X. Wang, B. A. Wallace and M. S. P. Sansom, HOLE: A program for the analysis of the pore dimensions of ion channel structural models, *J. Mol. Graphics*, 1996, **14**, 354–360.

49 Y.-Y. Jia, J.-C. Yin, N. Li, Y.-H. Zhang, R. Feng, Z.-Q. Yao and X.-H. Bu, Crystalline-State Solvent: Metal-Organic Frameworks as a Platform for Intercepting Aggregation-Caused Quenching, *Chin. J. Chem.*, 2022, **40**, 589–596.

50 J. Hafner, *Ab initio* simulations of materials using VASP: Density-functional theory and beyond, *J. Comput. Chem.*, 2008, **29**, 2044–2078.

51 J. P. Perdew, K. Burke and M. Ernzerhof, Generalized Gradient Approximation Made Simple, *Phys. Rev. Lett.*, 1996, **77**, 3865–3868.

52 G. Kresse and J. Furthmüller, Efficient iterative schemes for *ab initio* total-energy calculations using a plane-wave basis set, *Phys. Rev. B: Condens. Matter Mater. Phys.*, 1996, **54**, 11169–11186.

53 P. E. Blöchl, Projector augmented-wave method, *Phys. Rev. B: Condens. Matter Mater. Phys.*, 1994, **50**, 17953–17979.